

An asymmetric explosion mechanism may explain the diversity of Si II linewidths in Type Ia supernovae

Ran Livneh,¹★ Boaz Katz¹

¹*Department of Particle Physics & Astrophysics, The Weizmann Institute of Science, Rehovot 76100, Israel*

Accepted XXX. Received YYY; in original form ZZZ

ABSTRACT

Near maximum brightness, the spectra of Type Ia supernovae (SNe Ia) present typical absorption features of Silicon II observed at roughly 6100Å and 5750Å. The 2-D distribution of the pseudo-equivalent widths (pEWs) of these features is a useful tool for classifying SNe Ia spectra (Branch plot). Comparing the observed distribution of SNe on the Branch plot to results of simulated explosion models, we find that 1-D models fail to cover most of the distribution. In contrast, we find that TARDIS radiative transfer simulations of the WD head-on collision models along different lines of sight almost fully cover the distribution. We use several simplified approaches to explain this result. We perform order-of-magnitude analysis and model the opacity of the Si II lines using LTE and NLTE approximations. Introducing a simple toy model of spectral feature formation, we show that the pEW is a good tracer for the extent of the absorption region in the ejecta. Using radiative transfer simulations of synthetic SNe ejecta, we reproduce the observed Branch plot distribution by varying the luminosity of the SN and the Si density profile of the ejecta. We deduce that the success of the collision model in covering the Branch plot is a result of its asymmetry, which allows for a significant range of Si density profiles along different viewing angles, uncorrelated with a range of ⁵⁶Ni yields that cover the observed range of SNe Ia luminosity. We use our results to explain the shape and boundaries of the Branch plot distribution.

Key words: supernovae: general – radiative transfer

1 INTRODUCTION

There is strong evidence that Type Ia supernovae (SNe Ia) are the product of thermonuclear explosions of white dwarfs (WDs), yet the nature of the progenitor systems and the mechanism that triggers the explosion remain long-standing open questions (see e.g. Maoz et al. 2014; Livio & Mazzali 2018; Soker 2019 for recent reviews). Optical spectra at the photospheric phase are a sensitive probe of the structure and composition of SNe Ia ejecta. The P-Cygni absorption lines (superimposed upon a pseudo-continuum) are Doppler shifted and widened and their shape is directly related to the velocity distribution of the absorbing ions. The observed spectra show significant diversity in line depths (e.g. Branch et al. 2006), shifts (e.g. Wang et al. 2009) and time evolution (e.g. Benetti et al. 2005) which is partly correlated with the luminosity that covers a range of about one order of magnitude. Whether the observed diversity is a result of multiple explosion mechanisms or due to a continuous range

of underlying parameters in a single explosion mechanism is a key question in addressing the Type Ia problem.

Two especially useful features in the near-peak spectra of SNe Ia are the Si II features at 5750Å and 6100Å, attributed to Si II λ 5972 and Si II λ 6355. The 2-D distribution of the pseudo-equivalent widths (pEW) of these features (see Fig. 1) was introduced by Branch et al. (2006), classifying spectra into four groups: core normal (CN), broad line (BL), cool (CL), and shallow silicon (SS). It was shown that adjacent SNe on the plot exhibit overall similar spectra at maximum light, indicating that the variation in the two pEWs captures most of the observed diversity in near-peak spectra. The 6100Å feature spans a large range of pEWs (20Å to 200Å) while the 5750Å feature spans a smaller range (0 to 70Å) and the two pEWs are not correlated (though the range of 6100Å pEWs decreases with increasing pEW of the 5750Å feature). The span in observed pEWs is affected by the presence of Si at varying velocities and by the properties of the radiation field and electron density that determine the ionization and excitation level of the ions.

In order to relate the spectral features to the structure of explosion models, it would be useful to relate them to the

★ E-mail: ran.livneh@weizmann.ac.il

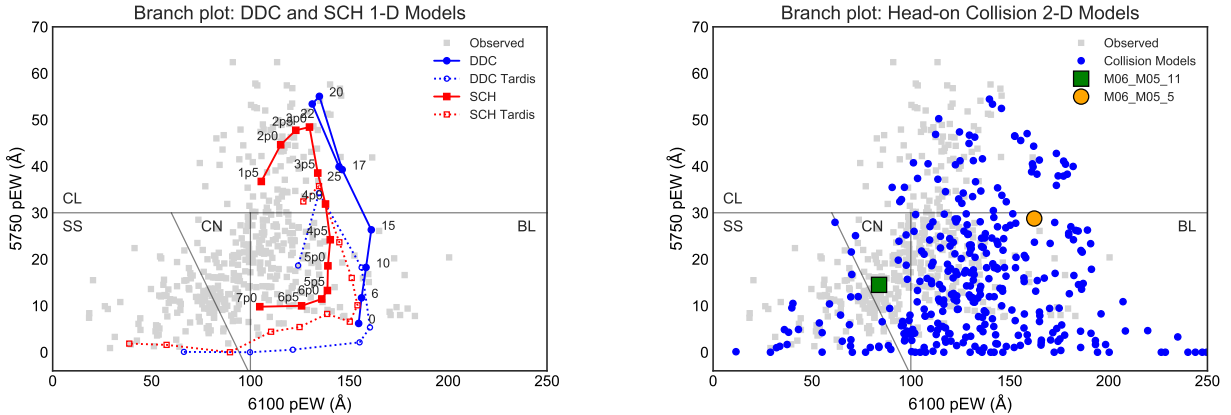


Figure 1. Branch plot of simulated models overlaid on observed CfA (Blondin et al. 2012), CSP (Folatelli et al. 2013) and BSNIP (Silverman et al. 2012) data (± 5 days from peak). Borders between Branch types follow Silverman et al. (2012). **Left:** Solid blue and red lines represent 1-D delayed detonation (DDC) and sub-Chandrasekhar models (SCH, see §4.2.1). The pEWs were extracted from numerically calculated spectra from Blondin et al. (2013, 2017). Model parameters can be found in Table 2. Dotted lines are the same models with radiative transfer simulated using TARDIS (this work). **Right:** Head-on direct collision models (Kushnir et al. 2013) with radiative transfer simulated using TARDIS for different viewing angles (§4.2.2). Two viewing angles of the same collision event between a $0.6M_{\odot}$ and a $0.5M_{\odot}$ WD with $M(^{56}\text{Ni}) = 0.27M_{\odot}$ are highlighted in green and orange (see Fig. 5). Corresponding Si density profiles are shown in the same colors in Fig. 2.

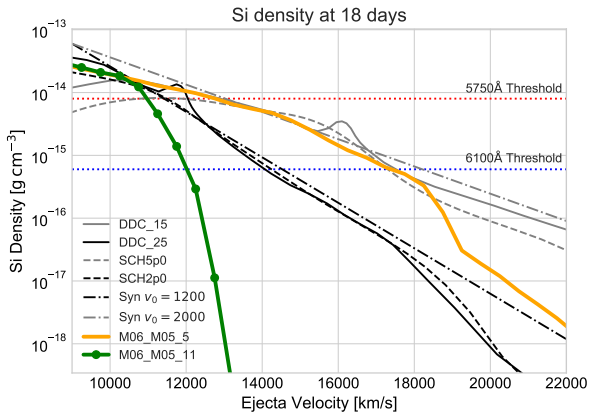


Figure 2. Si density at 18 days, as a function of velocity within the ejecta for various models: delayed detonations (DDC), sub-Chandrasekhar (SCH) (see §4.2.1), synthetic exponential (Syn, see §4.3) and head-on collisions (§4.2.2). Two examples are shown for each model. For the head-on collision model, two viewing angles of the same collision are shown (angle no. 5 and 11), in correspondence with Fig. 1 and Fig. 5. In M06_M05_5 the Si is extended whereas in M06_M05_11 the Si density drops steeply. The blue and red dotted lines are approximate Si density thresholds above which $\tau_s > 1$ for the 6100Å and 5750Å features, derived in §5.

distribution of Si in the ejecta. However, the fraction of Si in the relevant ionization (single) and excitation levels is of the order of 10^{-9} (see §2.1), and the optical depth depends on the properties of the plasma. In fact, the ratio of the depth of the two features is correlated with brightness in a continuous way (Nugent et al. 1995) and is understood to be set by the temperature which is largely determined by the luminosity (e.g. Hachinger et al. 2008). Using the photospheric spectral synthesis code TARDIS (Kerzendorf & Sim 2014), it

was recently shown by Heringer et al. (2017) that sequences of ejecta with the same structure and composition but with varying luminosities can (approximately) continuously connect the spectra of bright and faint Type Ia's. While these results demonstrate the role of the variations in the radiation field and strengthen the case for a single underlying mechanism, it is clear that the distribution of spectral features does not constitute a one-parameter family set by luminosity alone (e.g. Hatano et al. 2000).

As an illustration, the results of two main classes of spherically symmetric models that span the entire range of luminosities of Type Ia's are shown in the left panel of Fig. 1 based on the results of Blondin et al. (2013, 2017) – central detonations of sub-Chandrasekhar WDs (e.g. Sim et al. 2010) and delayed detonation Chandrasekhar models (e.g. Nomoto 1982; Khokhlov 1991). As can be seen, while the Si II line pEWs are in the right ball-park, they tend to the right side of the plot and cannot account for the 2-D distribution of observed pEWs. An exhaustive comparison of existing 1-D models is beyond the scope of this paper, but see for another example Fig. 16 of Wilk et al. (2018), where various 1-D model results are clustered near the BL region of the plot. Specifically, core normal (CN) SNe Ia are especially challenging to reproduce (e.g. Townsley et al. 2019).

In this paper we extend the study of Heringer et al. (2017) using similar approximations (in particular the TARDIS code), but including varying ejecta structures, and accounting for NLTE effects critical for quantitative analysis of the 5750Å feature. In particular, we show that a single asymmetric explosion model, namely head-on collisions of WDs (e.g. Rosswog et al. 2009, Raskin et al. 2010, Kushnir et al. 2013), can reach the entire extent of the observed distribution of line pEWs (see right panel of Fig. 1). This is due to the significant range of Si density profiles (see Fig. 2), which include profiles with Si extending to 20,000 km/s, but also profiles with sharp cutoffs at $v \lesssim$

13,000 km/s, depending on the viewing angle. The same collision models, when averaged over viewing angle and simulated as 1-D models, show only extended Si profiles and tend to the right side of the Branch plot (not plotted) like the other tested models. The head-on collision model is used here to demonstrate the possible role of asymmetry in reproducing the observed Branch plot.

An accurate calculation of the pEWs of the Si II features requires a self-consistent solution of the radiation transfer problem, coupled to the solution at each location of the ionization balance and the level excitation equilibrium, which deviate from local-thermal-equilibrium (LTE). TARDIS adopts crude approximations for the radiation field and ionization balance (while solving the non-LTE excitation equations, see §4). For this reason, our results should be treated as a proof-of-concept rather than as accurate estimates. A rough estimate of the accuracy is obtained by the comparison of our TARDIS calculations for the same ejecta as those used by Blondin et al. (2013, 2017), who solve the radiation transfer problem directly, which is shown in the left panel of Fig. 1. As can be seen, while there are significant differences for each ejecta, the sequence is qualitatively similar, with larger differences at higher temperatures (bottom of the plot, see §4.2.1).

The outline of this paper is as follows: In §2 an order-of-magnitude analysis of the formation of the Si II features is performed. In §3, a toy model of an ejecta containing a single, fully absorbing line is simulated. The resulting spectral features are shown to reproduce the non-trivial relations between the pEW and both the fractional depth and the FWHM. In §4 we describe our use of the TARDIS radiative transfer simulation and present results for several hydrodynamic models and synthetic ejecta, exploring the dependence of the Si features on ejecta composition and SN luminosity. In §5 we use our model to numerically find an approximate Si density threshold predicting the extent of the absorption region and the pEW of the 6100Å feature. Finally, in §6 we use our results to explain the boundaries of the Branch plot.

The observed SNe sample used in this paper is based on data from the Center for Astrophysics Supernova Program (CfA, Blondin et al. 2012), the Carnegie Supernova Project (CSP, Folatelli et al. 2013), and the Berkeley Supernova Ia Program (BSNIP, Silverman et al. 2012). We also use fractional depths and FWHM data from BSNIP in our study of the behavior of spectral features.

2 BASIC PROPERTIES OF THE TWO Si II FEATURES

In this section, we review the basic properties of the 6100Å and 5750Å features and explore their relation to typical properties of Type Ia supernovae.

2.1 Required density of excited Si II ions for absorption

The Sobolev optical depth for interaction is set by the local number density n_l of the ions in the lower excitation state of the transition. The required number density and mass density of Si ions in the lower excited level for a Sobolev

Wavelength (Å)	Transition	f	g_l	E_l (eV)
6371	7 → 11	0.414	2	8.121
6347	7 → 12	0.705	2	8.121
5957	11 → 15	0.298	2	10.066
5978	12 → 15	0.303	4	10.073

Table 1. Approximate parameters for the two Si II doublets (see inset, Fig. 3). Data from NIST (Kramida et al. 2019).

optical depth of unity at a time $t_{\text{exp}} = 18 t_{18\text{d}}$ days after explosion and transition wavelength of $\lambda \approx 6000$ Å are about:

$$n_{l,\text{min}} = \frac{1}{\lambda r_e t_{\text{exp}} c \pi f} \sim 0.4 f^{-1} t_{18\text{d}}^{-1} \text{ cm}^{-3}$$

$$\rho_{l,\text{min}} = 28 m_p n_{l,\text{min}} \sim 2 \times 10^{-23} f^{-1} t_{18\text{d}}^{-1} \text{ g cm}^{-3} \quad (1)$$

where f is the oscillator strength of the transition (see Table 1), $r_e = e^2/(m_e c^2)$ is the classical radius of the electron and the correction for stimulated emission is ignored.

The required density of excited ions is smaller by orders of magnitude than the typical density of a Type Ia expanding at $v = 10^9 v_9$ cm/s at similar epochs (see Fig. 2),

$$\rho \sim \frac{M_\odot}{\frac{4\pi}{3}(vt_{\text{exp}})^3} \sim 10^{-13} v_9^{-3} t_{18\text{d}}^{-3} \text{ g cm}^{-3}. \quad (2)$$

This does not always result in high optical depth however, since only a very small fraction of the Si is in the required ionization and excitation states as demonstrated below.

2.2 Rough estimates using the LTE approximation

A zeroth-order estimate of the fraction of Si in the correct ionization and excitation level can be obtained by assuming LTE, solving the Saha equation for the ionization and finding the excitation fractions from the Boltzmann distribution. The 6100Å and 5750Å features arise from the (doublet) transitions $3s^2 4s \rightarrow 3s^2 4p$ with rest-frame wavelength 6355Å and $3s^2 4p \rightarrow 3s^2 5s$ with rest-frame wavelength 5972Å, respectively, which are blue-shifted by about 10,000 km/s (see inset of Fig. 3 and Table 1). The density of Si II in the lower excitation levels for the two transitions assuming LTE is shown in dashed lines in Fig. 3 as a function of temperature for an adopted total density of $\rho = 6 \times 10^{-14} \text{ g cm}^{-3}$ and composition by mass of 60% Si, 30% S, 5% Ca, 5% Ar (e.g. similar to Nomoto et al. 1984) (elements other than Si having a weak effect on the free electron density and ionization). The required density for obtaining a Sobolev optical depth equal to unity at 18 days for the two features based on equations (1) is shown in Fig. 3 in blue and red dotted lines.

The photospheric temperature for typical luminosities of $L = 10^{43} L_{43} \text{ erg s}^{-1}$ is of order:

$$T_{\text{eff}} = \left(\frac{L/r_{\text{ref}}}{4\pi(vt_{\text{exp}})^2 \sigma_B} \right)^{1/4} \sim 10400 L_{43}^{1/4} v_9^{-1/2} t_{18\text{d}}^{-1/2} r_{0.5}^{-1/4} \text{ K} \quad (3)$$

where $r_{\text{ref}} = 0.5 r_{0.5}$ is the (inverse) suppression of the luminosity compared to that of a free surface due to the reflection of many of the photons back to the photosphere. As can be

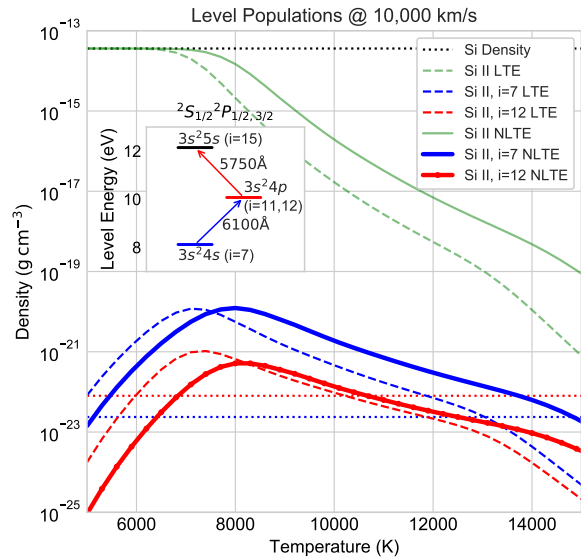


Figure 3. Density of Si II ions excited to the levels relevant for the 6100Å and 5750Å lines ($i = 7, 12$ – only one line from each doublet is shown) as a function of temperature. Total density is $\rho = 6 \times 10^{-14} \text{ g cm}^{-3}$ at 10,000 km/s (black dotted line) and the elemental abundance is taken to be 60% Si, 30% S, 5% Ca, 5% Ar. Green lines represent total Si II density, blue lines represent the density of Si II ions excited to the lower level of the 6100Å transition and red lines are the same for the 5750Å transition. Dashed lines are at LTE; solid lines assume nebular ionization with a dilution factor of $W = 0.3$ and are based on a detailed calculation of NLTE excitation equilibrium. Dotted blue and red lines represent the necessary n_I for $\tau_s = 1$ at 18 days without stimulated emission. The inset summarizes the 6100Å and 5750Å transitions.

seen in the figure, the typical density of ions for the relevant temperature of 10,000 K is about 10 to 100 times the required density for optical depth of unity. Given that the Si density naturally drops by more than 2 orders of magnitudes between 10,000 km/s and 20,000 km/s, it is reasonable that Type Ia’s have absorption regions that are within this range.

As can be seen in Fig. 3, at temperatures below about 7000 K, all Si atoms are singly ionized (Si II, green dashed line). For higher temperatures, the abundance of Si II diminishes quickly, giving way to doubly ionized Si III. An opposite effect occurs for the excitation – as the temperature rises, the higher excited levels which are necessary for the 5750Å and 6100Å transitions are increasingly populated. The combined effect of ionization and excitation is that for cooler ejecta (down to $\sim 7000 \text{ K}$ at V_{ph}), the optical depth τ_s at the photosphere of both lines is larger (see also Hachinger et al. 2008). As one moves out through the ejecta, the density drops, causing the optical depth to decrease, finally dropping below unity at a critical velocity affected by the initial value at the photosphere. For lower temperatures at the photosphere, the extent of the absorption region is increased, resulting in a larger pEW. Below a critical temperature of $\sim 7000 \text{ K}$ (for LTE) we identify a saturation effect: the popu-

lation of both of the relevant excited levels peaks and drops for lower temperatures. The implications of this effect will be discussed in §4.3.2.

3 TOY MODEL FOR SPECTRAL FEATURES

3.1 A simple absorption model reproduces relations between line parameters

The shape of an absorption line can be roughly described by two parameters: the maximal fractional depth (a) and the full-width at half-maximum (FWHM). The observed relations between these parameters and the pEW of the Si II features are shown in the top panels of Fig. 4 for the BSNIP (Silverman et al. 2012) sample of Type Ia supernovae near peak (± 5 days from peak). As can be seen, the FWHM and fractional depth are correlated with the pEW in a non-trivial way: for small pEWs ($\text{pEW} \lesssim 100\text{Å}$), the FWHM is approximately constant while the depth grows linearly with the pEW. For large pEWs the depth saturates and the FWHM grows with the pEW.

In order to study these relations we consider a simple spherical toy model: A photosphere expanding at $V_{\text{ph}} = 9,000 \text{ km/s}$ emits a flat spectrum and is surrounded by a shell with an infinite Sobolev optical depth $\tau_s = \infty$, with each interaction resulting in an (isotropic) scattering. Note that since photons are continuously red-shifted with respect to the rest-frame of the expanding plasma, each photon will (effectively) interact only once with a given transition. The shell extends from the photosphere to an outer velocity V_{shell} which sets the pEW of the line and is varied from 9,500 to 23,500 km/s to account for the observed range of pEWs. The resulting absorption feature shapes are generated using a Monte-Carlo calculation (5×10^8 photons per spectrum) and shown in the bottom-left panel of Fig. 4.

Here and throughout this study, feature parameters are extracted as follows (similar to the procedure described in Silverman et al. 2012): First, the spectrum is passed through a Savitzky-Golay filter (Savitzky & Golay 1964). Next, the endpoints of the feature are located – the feature is scanned from its minimum to both sides until a maximum is reached (with additional filtering at this stage). The pseudo-continuum is defined as a line passing through the two endpoints, and the spectrum is normalized by this pseudo-continuum (examples of pseudo-continuum lines can be seen in Fig. 6). The pEW is determined by integrating the outcome of the normalized feature spectrum subtracted from unity. The fractional depth and FWHM are also extracted from the normalized spectrum.

The resulting feature parameters obtained with this toy model are shown in the top panels of Fig. 4 for 3 choices of photospheric velocity V_{ph} . We suspect that the remaining difference between this simple model and the observations can be bridged by using a smoothly declining density profile, and introducing extra flux due to electron scattering in the ejecta. This is demonstrated by the dotted curve, derived from a similar model with $V_{\text{ph}} = 9,000 \text{ km/s}$ and a smooth exponentially declining optical depth of the form $\tau = \frac{1}{2} e^{-\frac{v-v_{\text{shell}}}{v_0}}$ with $v_0 = 1000 \text{ km/s}$, along with an addition of 20% white noise emulating flux due to electron scattering. As can be seen, the toy model recovers the relations between

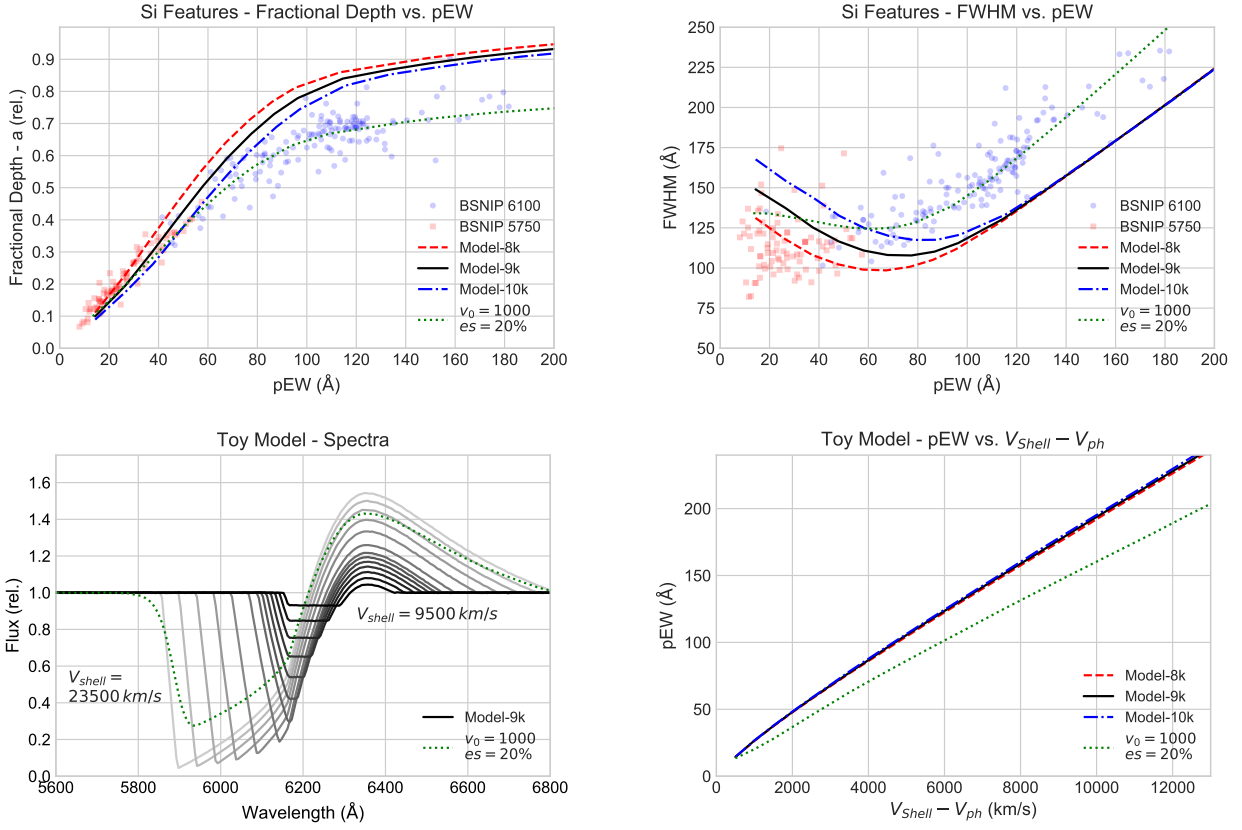


Figure 4. Relations between feature parameters in measured BSNIP (Silverman et al. 2012) data compared with simple toy models with $V_{\text{ph}} = 8, 9, 10 \times 10^3$ km/s and a varying (step-function) V_{shell} , and one toy model with $V_{\text{ph}} = 9 \times 10^3$ km/s and a smooth exponentially declining optical depth plus electron scattering flux (see §3.1). **Top:** Fractional depth and FWHM vs. pEW – BSNIP measurements for 6100Å and 5750Å features (blue and red dots) ± 5 days from peak and toy model results. **Bottom left:** Resulting toy model spectra for $V_{\text{ph}} = 9 \times 10^3$ km/s with increasing V_{shell} : First the fractional depth grows until it nears a maximum value. During this phase, the FWHM decreases. After the fractional depth is saturated, the FWHM begins to increase. The dotted line shows an example of the exponentially declining model for $V_{\text{shell}} = 23,500$ km/s. **Bottom right:** In all toy models, the pEW of a feature grows almost linearly with the extent of the absorbing region $V_{\text{shell}} - V_{\text{ph}}$. The exponentially declining model has systematically lower pEWs due to the addition of 20% white noise emulating electron scattering flux.

the different absorption line parameters to a reasonable accuracy for these choices.

3.2 Line pEW measures extent of absorption region

The fact that this simple model captures the main statistical features of the shapes of the absorption lines provides support for the approximation of a photosphere and a single absorbing line. Results of other models simulated with TARDIS are shown in Fig. A1. All simulated models are consistent with the observed behavior.

As can be seen in the bottom-right panel of Fig. 4, in this simple model the pEW is insensitive to the entire distribution of Si II ions and is a good estimator for the extent of the absorption region for the entire range of values (unlike the FWHM and fractional depths which saturate at the extreme regimes).

Thus, to a first approximation, the pEW is a measure of the extent of the absorption region, within which the optical depth is larger than unity. In the following sections, we shall see how the extent of the absorption region of the Si II

features depends on the Si density profile and the luminosity of the supernova.

4 RADIATIVE TRANSFER USING TARDIS

In order to explore the parameters affecting the Branch plot, we use the photospheric spectral synthesis code TARDIS (Kerzendorf & Sim 2014). TARDIS is a Monte-Carlo radiation transfer code that solves for a steady-state radiation field in a spherically symmetric ejecta with a predefined photosphere. Energy packets are injected at the photosphere with a black body distribution, propagate through the ejecta, interact with the plasma via bound-bound transitions and electron scattering and form the observed spectra when they escape. In our study, we use TARDIS with the most detailed macroatom model. The ionization fractions and level populations are iteratively calculated using rough approximations for deviations from LTE as explained below.

4.1 Non-LTE

The ionization and excitation state of the plasma in TARDIS is calculated (with some corrections) by assuming that the radiation field is given by a diluted black body:

$$J_\nu = WB_\nu(T_R) \quad (4)$$

where the dilution factor W and radiation temperature T_R are calculated based on appropriate estimators from photon packets. The free electrons are assumed to have a temperature $T_e = 0.9T_R$. The ionization is calculated by solving a modified Saha equation following the `nebular` ionization approximation (based on [Mazzali & Lucy 1993](#)):

$$\frac{N_{i,j+1}n_e}{N_{i,j}} = D \left(\frac{N_{i,j+1}n_e}{N_{i,j}} \right)^{LTE(Saha)} \quad (5)$$

where D is an ansatz correction factor that depends on W , the electron to radiation temperature ratio T_e/T_R , the fraction of recombinations that go directly to the ground state for each ion and corrections to account for the dominance of locally created radiation at short wavelengths (see eq. 2 and 3 in [Kerzendorf & Sim \(2014\)](#)).

The excitation levels are found using the `dilute-lte` excitation mode where the population of excited states is equal to the Boltzmann (LTE) population multiplied by the dilution factor W (excluding metastable states which are set to the Boltzmann distribution). As an exception, the excitation levels of Ca II, S II, Mg II and Si II ions are calculated with a "full NLTE" treatment, by explicitly finding the steady-state solution to radiative and collisional excitation transition equations (using the diluted black-body radiation field and including correction factors for multiple interactions before escape for finite Sobolev optical depths). As shown in [Kerzendorf & Sim \(2014\)](#), this has a significant effect on the pEW of the 5750Å feature.

The effect of this approximate NLTE treatment on the level populations is calculated and presented in Fig. 3 based on the TARDIS implementation and atomic data by [Kurucz & Bell \(1995\)](#) adapted from CMFGEN ([Hillier & Miller 1998](#)), using a typical near-photospheric dilution factor of $W = 0.3$. The resulting NLTE densities for the relevant levels are shown in solid lines. As can be seen in the figure, the NLTE treatment does not change the qualitative dependence of the level populations on temperature but has a significant quantitative effect. Specifically, the saturation effect discussed in §2.2 now presents at ~ 8000 K.

4.2 Ejecta from SNe Type Ia explosion models

4.2.1 1-D Chandrasekhar-mass and sub-Chandrasekhar models

We use TARDIS to simulate radiative transfer through ejecta of spherically symmetric models from the literature. These include central detonations of sub-Chandrasekhar mass WD (SCH, [Blondin et al. 2017](#)) and delayed-detonations of Chandrasekhar-mass WD (DDC, [Blondin et al. 2013](#)) models with a range of ^{56}Ni spanning the Type Ia range. Relevant model parameters are given in Table 2. For simplicity, we use $V_{\text{ph}} = 9,000$ km/s as the photosphere velocity for all models (the exact value has limited effect on the qualitative analysis). Using parameters given by the above authors, we

Model	M_{tot} (M_\odot)	$M(^{56}\text{Ni})$ (M_\odot)	$t_{\text{rise}}(\text{bol})$ (days)	$L_{\text{bol}}^{\text{max}}$ (erg/s)
Chandrasekhar-mass delayed-detonation models				
DDC0	1.41	0.86	16.7	1.85 (43)
DDC6	1.41	0.72	16.8	1.57 (43)
DDC10	1.41	0.62	17.1	1.38 (43)
DDC15	1.41	0.51	17.6	1.14 (43)
DDC17	1.41	0.41	18.6	9.10 (42)
DDC20	1.41	0.30	18.7	6.65 (42)
DDC22	1.41	0.21	19.6	4.47 (42)
DDC25	1.41	0.12	21.0	2.62 (42)
Sub-Chandrasekhar-mass models				
SCH7p0	1.15	0.84	16.4	1.85 (43)
SCH6p5	1.13	0.77	16.6	1.71 (43)
SCH6p0	1.10	0.70	16.9	1.57 (43)
SCH5p5	1.08	0.63	17.1	1.42 (43)
SCH5p0	1.05	0.55	17.6	1.25 (43)
SCH4p5	1.03	0.46	17.7	1.08 (43)
SCH4p0	1.00	0.38	17.6	9.01 (42)
SCH3p5	0.98	0.30	17.2	7.34 (42)
SCH3p0	0.95	0.23	16.8	5.76 (42)
SCH2p5	0.93	0.17	16.5	4.36 (42)
SCH2p0	0.90	0.12	15.8	3.17 (42)
SCH1p5	0.88	0.08	15.0	2.26 (42)

Table 2. Properties of SNe Ia models adapted from [Blondin et al. \(2017\)](#). Numbers in parentheses correspond to powers of ten.

set the time from explosion to $t_{\text{rise}}(\text{bol})$ and set $L_{\text{bol}}^{\text{max}}$ as the target luminosity for each model.

We extract the Si II features' pEWs from both the original spectra (derived from the radiation transfer simulations presented in the original papers) and the spectra obtained using TARDIS. The results of both methods are shown in the left panel of Fig. 1. As can be seen in the figure, the results are qualitatively similar. While quantitative differences clearly exist, both methods place these models on the right side of the Branch plot, covering it only partially.

4.2.2 2-D Head-on collision models

We use TARDIS to simulate radiative transfer through ejecta derived from 2-D hydrodynamic simulations of head-on (zero impact parameter) collisions of CO-WDs. In [Kushnir et al. \(2013\)](#), collisions of (equal and non-equal mass) CO-WDs with masses 0.5, 0.6, 0.7, 0.8, 0.9 and 1.0 M_\odot were simulated, resulting in explosions that synthesize ^{56}Ni masses in the range of 0.1 M_\odot to 1.0 M_\odot . The models used in this study (excluding rare collisions with 1.0 M_\odot WDs) are summarized in Table 3.

In order to use the 1-D TARDIS package, each collision model ejecta was sliced into 21 viewing angles. An example can be seen in Fig. 5. In this example it is apparent that the collision model produces an asymmetric ejecta: for some viewing angles, the Si extends to 20,000 km/s, while for others the Si density drops steeply at approximately 12,000 km/s. From each viewing angle, a 1-D model was generated with the density and abundance values sampled along the section. The luminosity $L_{\text{bol}}^{\text{max}}$ and rise time $t_{\text{rise}}(\text{bol})$ were taken for each viewing angle from global 2-D LTE ra-

Model	M_1 (M_\odot)	M_2 (M_\odot)	$M(^{56}\text{Ni})$ (M_\odot)	$t_{\text{rise}}(\text{bol})$ (days)	$L_{\text{bol}}^{\text{max}}$ (erg/s)
Head-on collision models					
M05_M05	0.50	0.50	0.10	14.8	2.98 (42)
M055_M055	0.55	0.55	0.22	15.7	5.56 (42)
M06_M05	0.60	0.50	0.27	15.3	6.54 (42)
M06_M06	0.60	0.60	0.33	16.0	7.64 (42)
M07_M05	0.70	0.50	0.26	15.7	6.51 (42)
M07_M06	0.70	0.60	0.38	16.0	8.81 (42)
M07_M07	0.70	0.70	0.56	15.9	1.25 (43)
M08_M05	0.80	0.50	0.29	16.2	7.32 (42)
M08_M06	0.80	0.60	0.38	16.3	9.54 (42)
M08_M07	0.80	0.70	0.48	16.5	1.17 (43)
M08_M08	0.80	0.80	0.74	15.5	1.67 (43)
M09_M05	0.90	0.50	0.69	15.6	1.34 (43)
M09_M06	0.90	0.60	0.50	16.5	1.26 (43)
M09_M07	0.90	0.70	0.51	16.7	1.23 (43)
M09_M08	0.90	0.80	0.54	17.1	1.27 (43)
M09_M09	0.90	0.90	0.78	16.8	1.74 (43)

Table 3. Properties of SNe Ia head-on collision models adapted from Kushnir et al. (2013). Numbers in parentheses correspond to powers of ten. $L_{\text{bol}}^{\text{max}}$ and $t_{\text{rise}}(\text{bol})$ represent averages over all viewing angles (see §4.2.2). Detailed values are provided in the supplementary files and show a standard deviation of $\sim 5\%$ for $t_{\text{rise}}(\text{bol})$ and $\sim 10\%$ for $L_{\text{bol}}^{\text{max}}$ across viewing angles.

diation transfer simulations of the same ejecta performed by Wygoda, N. (private communication) using a 2-D version of the URILIGHT radiation transfer code (Wygoda et al. 2019b, Appendix A). Average values are given in Table 3, and detailed values are available in the supplementary files. The inner boundary of the simulation was set at $V_{\text{ph}} = 9,000$ km/s for all models.

The resulting Branch plot distribution is shown in the right panel of Fig. 1. Remarkably, we find that the model covers most of the observed Branch plot distribution. A comparison of two models with the same ^{56}Ni yield but different Si density profiles (M06_M05_11 and M06_M05_5, see Figs. 2 and 5) shows the correspondence between the Si density profile and the position on the Branch plot. Examples of resulting spectra compared to observed spectra are presented in Appendix B.

We note that the construction presented here is not assumed to be exact. The method of taking a section of a 2-D model and producing from it a 1-D model is not equivalent to 2-D radiation transfer. However, the shape of absorption features depends mainly on the composition of material in the line of sight. Thus, the qualitative result that the collision model covers most of the Branch plot will likely hold. Additionally, actual collisions will cover a range of impact parameters and result in 3-D ejecta that are unavailable at this time.

4.3 Exploring synthetic ejecta

In this section, we apply the TARDIS radiative transfer simulation to synthetic ejecta models. This allows an exploration of the dependency of the Branch plot distribution on the properties of the ejecta in a controlled manner. We use simple exponentially declining density models of the

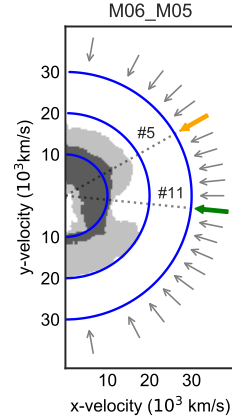


Figure 5. Si density map of a head-on collision model ejecta. Here a $0.6 M_\odot$ WD collides with a $0.5 M_\odot$ WD. The collision axis is the y-axis. The arrows represent simulated viewing directions. The orange and green arrows represent viewing angles 5 and 11 in correspondence with Fig. 1 and Fig. 2. The darker area represents regions with Si density $> 8 \times 10^{-15} \text{ g cm}^{-3}$ at 18.0 days after explosion. The lighter area is the same with Si density $> 6 \times 10^{-16} \text{ g cm}^{-3}$ (see §5).

form: $\rho(v) = \rho_0 e^{-v/v_0}$ up to a maximal velocity v_{max} . We use the same elemental abundance as in §2.2. We maintain a typical density for ejecta at maximum light at the photosphere ($\rho = 10^{-13} \text{ g cm}^{-3}$ at $V_{\text{ph}} = 9,000$ km/s at 18 days). We vary: (1) the target output luminosity (equivalent to $0.15 < M(^{56}\text{Ni})/M_\odot < 1.0$); (2) the e-folding of the exponent ($500 \text{ km/s} < v_0 < 2,500 \text{ km/s}$) and (3) the maximum velocity of the ejecta ($10,000 \text{ km/s} < v_{\text{max}} < 30,000 \text{ km/s}$). Fig. 6 shows example results of two such models.

Fig. 7 shows the resulting Branch plots overlaid on observed data. In the left panel, the maximum ejecta velocity is kept constant at $v_{\text{max}} = 30,000$ km/s. The different lines connect points of constant v_0 and varying luminosity (represented as $M(^{56}\text{Ni})/M_\odot$). In the right panel, the e-folding velocity is kept constant at $v_0 = 2,500$ km/s. The different lines connect points of constant v_{max} and varying luminosity. Additional models in which only the Si density profile varies while the total density profile remains constant show very similar results (see Fig. C1). We identify several interesting effects:

4.3.1 Luminosity explains one dimension of the plot

Looking at both panels of Fig. 7, we see that for higher luminosities ($M(^{56}\text{Ni})/M_\odot > 0.2$), decreasing the target luminosity increases the 5750Å pEW and allows the model to climb higher in the Branch plot (see also Heringer et al. 2017).

Fig. 6 provides an instructive example of how the luminosity affects the extent of the absorption region and the pEW of the features. In the $v_0 = 2,000$ km/s, $M(^{56}\text{Ni}) = 0.2 M_\odot$ model, the luminosity is low, and the temperature at the photosphere is ~ 8000 K. The corresponding level populations are well above the $\tau_\nu = 1$ threshold (see §2.2), and thus the attenuation profiles of both features begin at 100%. In contrast, in the $v_0 = 1,000$ km/s, $M(^{56}\text{Ni}) = 0.6 M_\odot$ model,

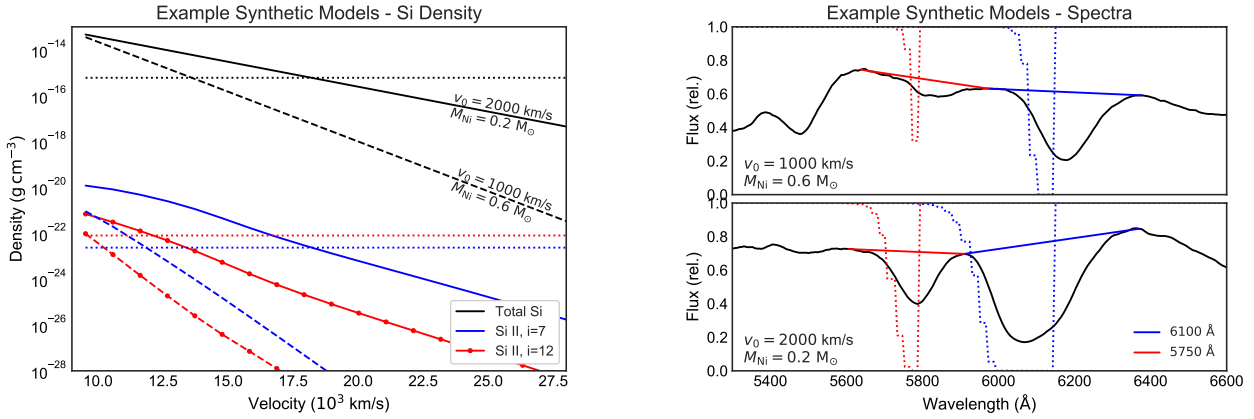


Figure 6. Results of TARDIS radiative transfer simulations on synthetic exponential density models of the form $\rho(v) = \rho_0 e^{-v/v_0}$, $\rho = 10^{-13} \text{ g cm}^{-3}$ at $V_{\text{ph}} = 9,000 \text{ km/s}$ at 18 days. Two models are shown as examples (marked with black circles in the left panel of Fig. 7). **Left:** Total Si density and density of Si II ions excited to the relevant levels. Solid lines represent a model with $v_0 = 2,000 \text{ km/s}$, $M(^{56}\text{Ni}) = 0.2 M_{\odot}$ and dashed lines represent a model with $v_0 = 1,000 \text{ km/s}$, $M(^{56}\text{Ni}) = 0.6 M_{\odot}$. Dotted blue and red lines represent the necessary n_I for $\tau_s = 1$ without stimulated emission (see Eqs. 1). The dotted black line represents the total Si density threshold obtained in §5 for the 6100Å feature. **Right:** Simulated spectra, including the automatic detection of the pseudo-continuum for the pEW calculation, with the original attenuation profile that generated the spectral features overlaid (dotted lines). The lower temperature at V_{ph} in the $v_0 = 2,000 \text{ km/s}$, $M(^{56}\text{Ni}) = 0.2 M_{\odot}$ model results in a higher population of both levels. Both this and the higher e-folding constant v_0 cause the absorption region to be more extended than in the second model, resulting in larger pEWs for both features.

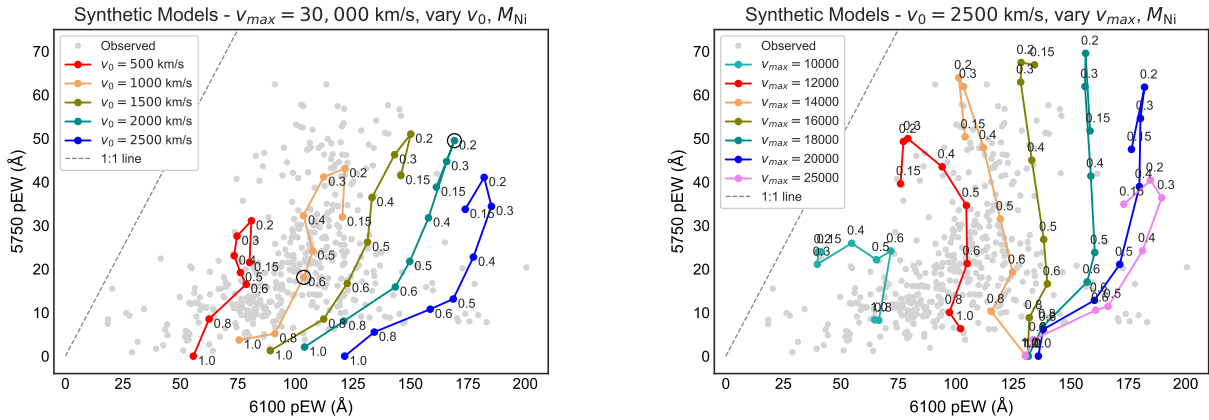


Figure 7. Simulated synthetic models with exponential density profiles of the form $\rho(v) = \rho_0 e^{-v/v_0}$, $\rho = 10^{-13} \text{ g cm}^{-3}$ at $V_{\text{ph}} = 9,000 \text{ km/s}$ at 18 days, overlaid on observed CfA, CSP and BSNIP data. $M(^{56}\text{Ni})$ is stated next to each point in units of M_{\odot} . L is computed from $M(^{56}\text{Ni})$ using Arnett's rule $L_{\text{max}} = 2.0 \times 10^{43} \times [M(^{56}\text{Ni})/M_{\odot}] \text{ erg/s}$. **Left:** Each line represents a constant e-folding velocity v_0 with varying luminosity. All models are simulated to $v_{\text{max}} = 30,000 \text{ km/s}$. Circles mark models corresponding to examples in Fig. 6. **Right:** Exponential synthetic models with a constant e-folding velocity $v_0 = 2,500 \text{ km/s}$. Each line represents a constant maximum ejecta velocity cutoff v_{max} with varying luminosity.

the luminosity is high, and the temperature at the photosphere is $\sim 10,000 \text{ K}$. As a result, the level populations are lower: the 6100Å feature begins at 100% attenuation, but the 5750Å feature begins at only 70% attenuation and drops quickly.

4.3.2 Lowering the luminosity further saturates both features

What happens when we further decrease the luminosity? As we can see in Fig. 7, it turns out that both features' pEW is limited due to the saturation effect shown in Fig. 3.

When the temperature near the photosphere declines to values lower than $\sim 8000 \text{ K}$, the ionization levels out but the excitation continues to decrease. For sufficiently low luminosities, the temperature at the photosphere drops below $\sim 8000 \text{ K}$, thus reducing the level populations, the optical depth, and ultimately the pEW of the features. A similar effect can also be identified in the DDC and SCH models shown in the left panel of Fig. 1.

4.3.3 Varying the e-folding velocity spans the width of the plot

Looking at the left panel of Fig. 7, we see that as the e-folding velocity v_0 is increased, the 6100Å pEW reaches higher values (Branch et al. 2009 obtained similar results using SYNOW). This can be explained using Fig. 6: in the $v_0 = 2,000$ km/s, $M(^{56}\text{Ni}) = 0.2 M_\odot$ model, the e-folding velocity v_0 is higher than in the $v_0 = 1,000$ km/s, $M(^{56}\text{Ni}) = 0.6 M_\odot$ model, thus the Si density profile is more extended. Consequently, the level populations go below the $\tau_s = 1$ threshold at a higher velocity, resulting in larger pEWs.

Are all of these density profiles physical? For an exponential density profile model for homologously expanding supernovae, $E = 6Mv_0^2$ (e.g. Jeffery 1999). Assigning a typical energy to mass ratio for nuclear processes $\frac{E}{M} \approx \frac{0.5 \text{ MeV}}{m_p}$, we obtain $v_0 \approx 2,800$ km/s. According to Fig. 7, this means that spherically symmetric models with an exponential density profile and constant abundance will tend to the right side of the Branch plot and will not be able to span the whole observed distribution. If this exponential model is representative, in order to cover the left side of the Branch plot, a model needs to produce viewing angles in which the Si density drops off more steeply than the total density.

4.3.4 Limiting the maximum velocity of the ejecta spans the width of the plot

Another demonstration of the ability to span the horizontal dimension of the plot by narrowing the absorption region is achieved by taking a synthetic ejecta with $v_0 = 2,500$ km/s (close to the $v_0 \approx 2,800$ km/s obtained in the previous section) and cutting it off at various velocities v_{max} . The results of this approach are shown in the right panel of Fig. 7.

Noticing that this method achieves a fuller coverage of the observed Branch plot, we conclude that the top left side of the plot, namely a high 5750Å pEW with a low 6100Å pEW, can be reached with this type of exponential model if a cut off in the Si profile exists at $v_{\text{max}} \approx 12,000$ km/s.

5 SI DENSITY THRESHOLDS

Using the NLTE model described in §4.1, we numerically find the Si density corresponding to $\tau_s = 1$ for various temperatures and velocities in the ejecta, assuming a dilution factor with geometric dependence on velocity $W = [1 - (1 - (V_{\text{ph}}/v)^2)]^{1/2}/2$. The results are shown in dashed (6100Å) and dashed-dotted (5750Å) lines in Fig. 8.

For low luminosity models, within the range 7,000 K to 9,500 K and velocities $10,000 \text{ km/s} < v < 20,000 \text{ km/s}$, the Si density required for $\tau_s = 1$ spans only one order of magnitude. Thus, we attempt to set total Si density thresholds of $\rho_{6100} = 6 \times 10^{-16} \text{ g cm}^{-3}$ for the 6100Å feature, and $\rho_{5750} = 8 \times 10^{-15} \text{ g cm}^{-3}$ for the 5750Å feature (solid lines in Fig. 8) for obtaining significant optical depth, in the hope that they are applicable to most relevant conditions.

In order to test the predictive power of the thresholds obtained above, we find the intersection of the ρ_{6100} threshold with the Si density profiles of all of the models presented in this paper to obtain effective "maximum Si velocities". These are plotted against the 6100Å pEWs in Fig. 9. The

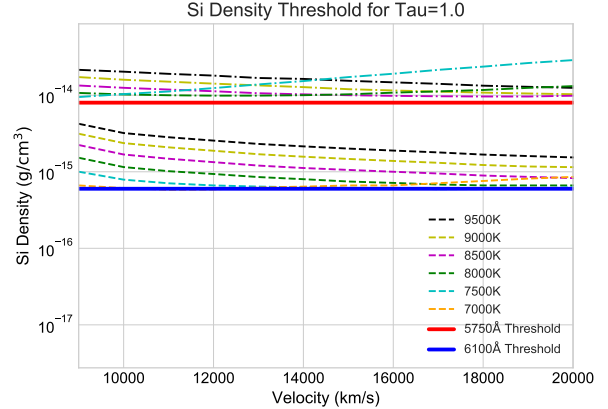


Figure 8. Total Si density necessary to obtain $\tau_s = 1$ is iteratively computed for different temperatures and velocities, assuming a geometric dilution factor ($W = [1 - (1 - (V_{\text{ph}}/v)^2)]^{1/2}/2$) within the ejecta. Temperatures shown for dashed lines for the 6100Å feature, apply to same colored dash-dotted lines for the 5750Å feature. Minimal thresholds (ρ_{5750} , ρ_{6100}) are marked in bold lines.

dotted line in the figure represents the $V_{\text{ph}} = 9,000$ km/s toy model of §3. The head-on collision and synthetic models show a correlation similar to the toy model, especially for low luminosity models, as would be expected from Fig. 8. On the other hand, the delayed-detonation and sub-Chandrasekhar models do not display a similar correlation. In both of these models, the luminosity is correlated with the extent of the Si density profile, and so they lack ejecta with high "maximum Si velocity" and low luminosity. A possible solution is defining a threshold that is a function of luminosity.

Also shown in Fig. 9 are green and orange circles representing two viewing angles of the M06_M05 head-on collision model (see Fig. 5). Fig. 2 shows the Si density profiles of these models and their intersection with the ρ_{6100} threshold. M06_M05_11 (in green) drops steeply and intersects ρ_{6100} at $\sim 12,000$ km/s whereas M06_M05_5 (in orange) is more extended. A comparison with the right panel of Fig. 1 shows the correspondence between the intersection velocity and the position on the Branch plot.

A similar exercise for the ρ_{5750} threshold does not produce useful results. The Si density profiles tend to be flat close to the photosphere where this feature is formed (see Fig. 2) and the uncertainty in the threshold entails a large variation in the effective "maximum Si velocity".

6 BOUNDARIES OF THE BRANCH PLOT

Based on the results of the previous sections, we can now attempt to explain the shape and boundaries of the observed Branch plot.

6.1 Top boundary

It is well known (e.g. Nugent et al. 1995; Heringer et al. 2017, §4.3.1) that as the SN luminosity decreases, the pEW of the 5750Å feature increases. It was shown however in §4.3.2

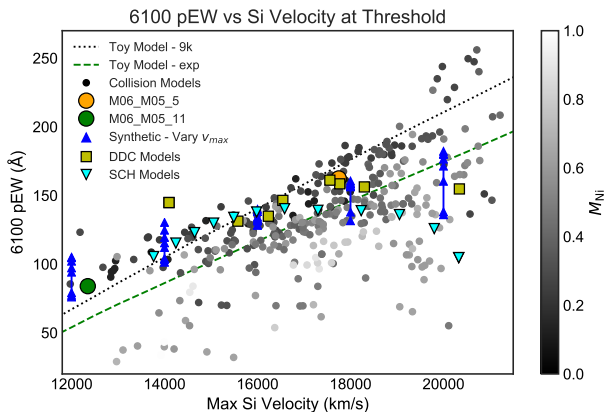


Figure 9. 6100Å pEW vs effective “maximum Si velocity” (at which Si density = ρ_{6100} , see §5) for various models. The head-on collision models are colored according to their $M(^{56}\text{Ni})$. Orange and green circles show the two extreme models in correspondence with Figures 1, 2 and 5. The dotted and dashed lines represent the $V_{\text{ph}} = 9,000$ km/s and exponential toy models in §3.

that there is a limit on the maximum pEW of the 5750Å feature due to the peak population of the Si II $i = 11, 12$ levels at $T \sim 8000$ K (see Fig. 3). Looking at Fig. 7, it seems that the largest 5750Å pEWs obtained with synthetic models generally match the largest observed pEWs, hinting that the maximal observed value may be related to this limit. On the other hand, ejecta with ^{56}Ni masses of $\sim 0.1 M_{\odot}$ at the lower end of the Type Ia brightness distribution have comparable 5750Å pEWs.

Thus, it is hard to distinguish between the top boundary of the observed Branch plot distribution as being (a) due to the physical limit on the lowest luminosity of SNe Ia events; or (b) due to the optical depth reaching a maximum value at some temperature as a result of the atomic physics.

Currently, plots of the Si II features’ pEW vs. luminosity tracers such as $\Delta m_{15}(\text{B})$ do not show a significant saturation effect (see e.g. Fig. 17 in Folatelli et al. 2013). Observations of lower luminosity SNe Ia may discover such an effect in the future.

6.2 Left boundary

Looking at Fig. 3, we can infer that the optical depth of the 6100Å transition is always larger than the optical depth of the 5750Å transition. In LTE this is always true given the values of the oscillator strengths and the higher energy of the lower level of the 5750Å transitions. Using the parameters in Table 1 and ignoring the correction for stimulated emission, we derive for LTE:

$$\frac{\tau_{5750}}{\tau_{6100}} \sim \frac{f_{\lambda 5957} g_{\lambda 5957} + f_{\lambda 5978} g_{\lambda 5978}}{f_{\lambda 6371} g_{\lambda 6371} + f_{\lambda 6347} g_{\lambda 6347}} e^{-\frac{\Delta E}{kT_R}} \lesssim e^{-\frac{2eV}{kT_R}} < 1 \quad (6)$$

We verified that this continues to hold after applying TARDIS’s NLTE corrections in the following relevant range of parameters: $0.005 < W < 0.5$, $5 \times 10^{-17} \text{ g cm}^{-3} < \rho < 1 \times 10^{-12} \text{ g cm}^{-3}$, and $5,000 \text{ K} < T < 20,000 \text{ K}$. Since these hold throughout the ejecta outside the photosphere, the pEW of the 6100Å feature will always be larger or equal to the

pEW of the 5750Å feature. This means that the 6100Å pEW will always be larger than the 5750Å pEW. Thus, the left boundary of the Branch plot is constrained by a 1:1 line (shown in Fig. 7).

The models closest to the 1:1 line will be ones with a steep Si density cutoff at low velocity. When this happens, both features begin at the photosphere with high attenuation and both stop at similar velocities. This allows the pEW of the 5750Å feature to approach the pEW of the 6100Å feature (see §4.3.4).

Fig. 2 shows Si density profiles of various models. The examples given of the SCH and DDC models resemble synthetic models with $v_0 = 1,200$ km/s and $v_0 = 2,000$ km/s. According to Fig. 7, they would tend to the right side of the Branch plot, and in the left panel of Fig. 1 we see that this is indeed the case. Again in Fig. 2, we see the Si density profile of a head-on collision model (M06_M05_11) that drops steeply at $\sim 12,000$ km/s. The right panel of Fig. 1 shows the same model on the left side of the Branch plot.

Another demonstration of this can be seen using the synthetic model in Fig. 7. In the left panel, the models’ density decreases exponentially, and the top-left region of the Branch plot remains out of reach. In the right panel, the density is cut abruptly at some v_{max} , allowing the models to cover this part of the Branch plot as well.

6.3 Right boundary

A possible limit on the 6100Å pEW could be interaction with the 5750Å feature. Looking at the bottom left panel of Fig. 4, we see that the P-Cygni profile increases the flux red-ward of the rest-frame interaction wavelength (although the toy model exaggerates this effect due to lack of electron scattering). The velocity difference between the two features is only $\sim 18,000$ km/s and thus interaction is possible. While in the head-on collision and synthetic models we did observe interaction and merging between features, in the observed sample the features appear to almost always be separated, so this effect is not understood to have a major effect on the shape of the right boundary.

A better explanation is that the limit on the 6100Å pEW arises from a physical limit on the maximum velocity of Si with $\tau_s > 1$ for the 6100Å absorption line. This is supported by the toy model presented in §3. The synthetic models of §4.3 show that this can be translated into a condition on the Si density profile in the ejecta – Fig. 7 shows that the 6100Å pEW is determined by the extent of the Si density profile.

However, looking at the left panel of Fig. 7, we see that the analytic e-folding velocity $v_0 \approx 2,800$ km/s discussed in §4.3.3 for an exponential density profile would result in 6100Å pEWs larger than the observed ones. We deduce from this that the Si density drops faster than the overall ejecta density in most SNe. This is indeed the case for all explosion models presented here (see representative examples in Fig. 2 for which the Si density profiles are all steeper than an exponent with $v_0 = 2000$ km/s, shown in a dashed-dotted gray line).

7 DISCUSSION

The observed Branch plot distribution is 2-dimensional, implying that 1-D models with a single variable parameter will not be able to reproduce it. This is demonstrated using the DDC and SCH models in the left panel of Fig. 1. Thus, the width of the Branch plot supports the claim that apart from luminosity, other physical parameters affect the spectra of SNe Ia (e.g. [Hatano et al. 2000](#)). Asymmetric explosion models may provide this additional degree of freedom by allowing uncorrelated variation of the luminosity and the Si density profile based on the selection of viewing angle.

In this paper we focus on the head-on collision model (e.g. [Rosswog et al. 2009](#); [Raskin et al. 2010](#)). This model has shown promising results in terms of explaining the detonation mechanism and accounting for the observed range of ^{56}Ni yields ([Kushnir et al. 2013](#)), reproducing the observed gamma-ray escape time ([Kushnir et al. 2013](#); [Wygoda et al. 2019a](#)) and explaining nebular spectra bi-modal emission features ([Dong et al. 2015](#); [Vallely et al. 2020](#)), while facing a growing challenge in accounting for the observed rate of SNe Ia (e.g. [Klein & Katz 2017](#); [Haim & Katz 2018](#); [Toonen et al. 2018](#); [Hamers 2018](#); [Hallakoun & Maoz 2019](#)). The full coverage of the Branch plot distribution, shown in the right panel of Fig. 1, provides further support for the collision model. We note that the resulting distribution does not reproduce the observed density of events across the plot, however such a comparison is premature, given that observational biases were not corrected for and 3-D ejecta spanning the range of non-zero impact parameters are not available. Other characteristics that have not been explored in this paper include the time-evolution and the velocities of the Si II features and the distribution of ^{56}Ni mass on the Branch plot.

Other asymmetric models that produce ejecta with a range of Si density profiles uncorrelated with luminosity may also cover the Branch plot distribution. As a recent example, in [Townesley et al. \(2019\)](#) a 2-D hydrodynamical simulation of a $1 M_{\odot}$ WD double-detonation model is shown to result in an off-center detonation that produces a SN Ia that is normal in its brightness and spectra, with significant variation in the Si density profile as a function of viewing angle. Further study is required to check the Branch plot distribution of a family of these models that reproduce the relevant range of ^{56}Ni yields.

Asymmetry in ejecta may offer an explanation for additional characteristics of SNe Ia, such as the variation in Si velocity gradients, bi-modal and shifted nebular spectral lines and the presence of high velocity features (e.g. [Maeda et al. 2010](#); [Blondin et al. 2011](#); [Childress et al. 2014](#); [Dong et al. 2015, 2018](#); [Maguire et al. 2018](#)). However, there are observational constraints that limit the possible degree of asymmetry of SNe Ia ejecta. The typically low observed continuum polarization is an important example (e.g. [Wang & Wheeler 2008](#); [Bulla et al. 2016a,b](#)). Further study is required to verify that an asymmetric origin for the spectral diversity of SNe Ia is consistent with other observed aspects. In particular, modeling of the polarization associated with the collision model is needed and is beyond the scope of this paper.

Several assumptions and approximations limit the quantitative accuracy of our results. Calculation of the

pEWs of the Si II features requires a self-consistent solution of the radiation transfer problem, coupled to the solution at each location of the ionization balance and the level excitation equilibrium, which deviate from local-thermal-equilibrium (LTE). We use TARDIS, which adopts crude approximations for the radiation field and ionization balance, affecting the expected accuracy of the simulations. In addition, the radiative transfer analysis of the 2-D collision models is performed by creating 1-D models with density and abundance sampled along sections of the 2-D ejecta from multiple viewing angles. This is not equivalent to 2-D radiation transfer. However, the shape of an absorption feature depends mainly on the composition of material in the line of sight. Thus, we believe the qualitative analysis presented here is correct. This can be verified in the future with improved NLTE treatment and 3-D simulations.

Another result, unrelated to the symmetry of SNe Ia ejecta, stems from our analysis of the level populations relevant for the creation of the Si II features (Fig. 3). These predict a peak of the population of the lower level of the 5750\AA transition at a photospheric temperature of $T \sim 8000\text{ K}$. In our simulated models, this leads to an upper limit on the 5750\AA pEW at low luminosities. This saturation effect also manifests in the other models mentioned in this paper, which are based on independent radiative transfer models (see left panel of Fig. 1). Currently, plots of the Si II features' pEW vs. luminosity tracers such as $\Delta m_{15}(\text{B})$ do not show a significant saturation effect (see e.g. Fig. 17 in [Folatelli et al. 2013](#)). If such an effect is identified in future observations of lower luminosity SNe it may help calibrate the photospheric temperature and provide a useful tool for constraining progenitor models.

8 SUMMARY

As part of the ongoing effort to identify the nature of the progenitor system of Type Ia supernovae, we study the spectra of these objects at maximum bolometric luminosity. We focus on the Si II 6100\AA and 5750\AA features and use the Branch plot, a 2-D plot of the pEW distribution ([Branch et al. 2006](#)), as a tool to test the validity of different models.

The main result of this paper is presented in Fig. 1, where the distribution of Si II pEWs for simulated hydrodynamical explosion models is compared to observations. The 1-D SCH and DDC models fail to reach most of the observed range of pEWs, while the head-on collision model shows almost full coverage of the observed distribution (for sample spectra see Appendix B). As shown in this paper, the success of the head-on collision model in reproducing the observed distribution on the Branch plot is a result of its asymmetry, which allows for a significant range of Si density profiles along different viewing angles (Fig. 2), coupled but uncorrelated with a range of ^{56}Ni yields that cover the observed range of SNe Ia luminosity.

An order-of-magnitude analysis of the formation of the Si II features is performed in §2. The Si density is shown to be 10 to 100 times the required density for optical depth of unity for these features (Fig. 3). Given that the Si density naturally drops by more than 2 orders of magnitudes between 10,000 km/s and 20,000 km/s, it is reasonable that Type Ia's have absorption regions that are within this range.

The population of the relevant Si II excited levels rises with decreasing temperature, explaining the dependence of the Si II pEWs on SN luminosity. The population peaks at $T \sim 8000$ K, causing a saturation effect (see §4.3.2) and predicting a maximum pEW at low luminosity.

In an attempt to clarify the effects of geometry on the spectral features, in §3 a toy model of an ejecta containing a single absorption line is simulated. The resulting spectral features are shown to reproduce the non-trivial relations between the pEW and both the fractional depth and the FWHM (Fig. 4). These results support our assumption that the Si II features can be analyzed as being due to a single absorption line, and show that the pEW is a good tracer for the extent of the absorption region.

In §4.3 TARDIS is applied to simplified synthetic ejecta with exponentially declining density models. The observed Branch plot distribution is reproduced by varying two factors: the luminosity of the SN and the Si density profile of the ejecta (Fig. 7). Specifically, introducing a cutoff to the Si density profile at low v_{\max} leads to Si II features located on the elusive top left part of the Branch plot.

Realizing the importance of the Si density profile, we numerically find an approximate Si density threshold, predicting the extent of the absorption region and the pEW of the 6100Å feature. The use of this threshold on sample ejecta is demonstrated in Fig. 9, showing a clear correlation between the effective "maximum Si velocity" in the ejecta and the 6100Å pEW for low luminosity head-on collision and synthetic models.

Based on the above results, the bounds of the Branch plot are explained: the top boundary represents either a limit on the lowest luminosity of SNe Ia events or a limit on the maximum optical depth from atomic physics due to the saturation effect (see §6.1). The left boundary is constrained by a 1:1 line from atomic physics (shown in Fig. 7), and it seems that for low-luminosity events to approach it requires a steeply falling Si density profile (§6.2). The right boundary represents an upper limit on the velocity of Si in the ejecta.

ACKNOWLEDGEMENTS

We thank Doron Kushnir and Stéphane Blondin for sharing model ejecta and spectra. We thank Nahliel Wygoda for sharing light-curve data. We thank Eli Waxman, Avishay Gal-Yam and Doron Kushnir for useful discussions. We thank Wolfgang Kerzendorf and other TARDIS contributors for their support. We thank the anonymous referee for helpful comments. This work was supported by the Beracha foundation and the Minerva foundation with funding from the Federal German Ministry for Education and Research. This research made use of TARDIS, a community-developed software package for spectral synthesis in supernovae (Kerzendorf & Sim 2014; Kerzendorf et al. 2019). The development of TARDIS received support from the Google Summer of Code initiative and from ESA's Summer of Code in Space program. TARDIS makes extensive use of Astropy and PyNE.

REFERENCES

Benetti S., et al., 2005, *ApJ*, **623**, 1011

- Blondin S., Tonry J. L., 2007, *ApJ*, **666**, 1024
- Blondin S., Kasen D., Röpke F. K., Kirshner R. P., Mandel K. S., 2011, *MNRAS*, **417**, 1280
- Blondin S., et al., 2012, *AJ*, **143**, 126
- Blondin S., Dessart L., Hillier D. J., Khokhlov A. M., 2013, *MNRAS*, **429**, 2127
- Blondin S., Dessart L., Hillier D. J., Khokhlov A. M., 2017, *MNRAS*, **470**, 157
- Branch D., et al., 2006, *Publications of the Astronomical Society of the Pacific*, **118**, 560
- Branch D., Chau Dang L., Baron E., 2009, *Publications of the Astronomical Society of the Pacific*, **121**, 238
- Bulla M., Sim S. A., Pakmor R., Kromer M., Taubenberger S., Röpke F. K., Hillebrandt W., Seitenzahl I. R., 2016a, *MNRAS*, **455**, 1060
- Bulla M., et al., 2016b, *MNRAS*, **462**, 1039
- Childress M. J., Filippenko A. V., Ganeshalingam M., Schmidt B. P., 2014, *MNRAS*, **437**, 338
- Dong S., Katz B., Kushnir D., Prieto J. L., 2015, *MNRAS*, **454**, L61
- Dong S., et al., 2018, *MNRAS*, **479**, L70
- Folatelli G., et al., 2013, *ApJ*, **773**, 53
- Hachinger S., Mazzali P. A., Tanaka M., Hillebrandt W., Benetti S., 2008, *MNRAS*, **389**, 1087
- Haim N., Katz B., 2018, *MNRAS*, **479**, 3155
- Hallakoun N., Maoz D., 2019, *MNRAS*, **490**, 657
- Hamers A. S., 2018, *MNRAS*, **478**, 620
- Hatano K., Branch D., Lentz E. J., Baron E., Filippenko A. V., Garnavich P. M., 2000, *ApJ*, **543**, L49
- Heringer E., van Kerkwijk M. H., Sim S. A., Kerzendorf W. E., 2017, *Astrophys. J.*, **846**, 15
- Hillier D. J., Miller D. L., 1998, *ApJ*, **496**, 407
- Jeffery D. J., 1999, arXiv e-prints, [pp astro-ph/9907015](https://arxiv.org/abs/astro-ph/9907015)
- Kerzendorf W. E., Sim S. A., 2014, *MNRAS*, **440**, 387
- Kerzendorf W., et al., 2019, tardis-sn/tardis: TARDIS v3.0 alpha2, [doi:10.5281/zenodo.2590539](https://doi.org/10.5281/zenodo.2590539), <https://doi.org/10.5281/zenodo.2590539>
- Khokhlov A. M., 1991, *A&A*, **245**, 114
- Klein Y. Y., Katz B., 2017, *MNRAS*, **465**, L44
- Kramida A., Yu. Ralchenko Reader J., and NIST ASD Team 2019, NIST Atomic Spectra Database (ver. 5.7.1), [Online]. Available: <https://physics.nist.gov/asd> [2019, December 5]. National Institute of Standards and Technology, Gaithersburg, MD.
- Kurucz R. L., Bell B., 1995, Atomic line list
- Kushnir D., Katz B., Dong S., Livne E., Fernández R., 2013, *ApJ*, **778**, L37
- Livio M., Mazzali P., 2018, *Phys. Rep.*, **736**, 1
- Maeda K., et al., 2010, *Nature*, **466**, 82
- Maguire K., et al., 2018, *MNRAS*, **477**, 3567
- Maoz D., Mannucci F., Nelemans G., 2014, *Annual Review of Astronomy and Astrophysics*, **52**, 107
- Mazzali P. A., Lucy L. B., 1993, *A&A*, **279**, 447
- Nomoto K., 1982, *ApJ*, **253**, 798
- Nomoto K., Thielemann F. K., Yokoi K., 1984, *ApJ*, **286**, 644
- Nugent P., Phillips M., Baron E., Branch D., Hauschildt P., 1995, *ApJ*, **455**, L147
- Raskin C., Scannapieco E., Rockefeller G., Fryer C., Diehl S., Timmes F. X., 2010, *ApJ*, **724**, 111
- Rosswog S., Kasen D., Guillochon J., Ramirez-Ruiz E., 2009, *ApJ*, **705**, L128
- Savitzky A., Golay M. J. E., 1964, *Analytical Chemistry*, **36**, 1627
- Silverman J. M., Kong J. J., Filippenko A. V., 2012, *MNRAS*, **425**, 1819
- Sim S. A., Röpke F. K., Hillebrandt W., Kromer M., Pakmor R., Fink M., Ruitter A. J., Seitenzahl I. R., 2010, *ApJ*, **714**, L52
- Soker N., 2019, arXiv e-prints, [p. arXiv:1912.01550](https://arxiv.org/abs/1912.01550)

- Toonen S., Perets H. B., Hamers A. S., 2018, *Astronomy & Astrophysics*, 610, A22
- Townsley D. M., Miles B. J., Shen K. J., Kasen D., 2019, *ApJ*, 878, L38
- Valley P. J., Tucker M. A., Shappee B. J., Brown J. S., Stanek K. Z., Kochanek C. S., 2020, *MNRAS*, 492, 3553
- Wang L., Wheeler J. C., 2008, *ARA&A*, 46, 433
- Wang X., et al., 2009, *ApJ*, 699, L139
- Wilk K. D., Hillier D. J., Dessart L., 2018, *MNRAS*, 474, 3187
- Wygoda N., Elbaz Y., Katz B., 2019a, *MNRAS*, 484, 3941
- Wygoda N., Elbaz Y., Katz B., 2019b, *MNRAS*, 484, 3951
- Yaron O., Gal-Yam A., 2012, *Publications of the Astronomical Society of the Pacific*, 124, 668

APPENDIX A: RELATIONS BETWEEN LINE PARAMETERS IN SIMULATED MODELS

The simple toy model presented in §3 and shown in Fig. 4 reproduces a crude approximation of the observed relations between feature parameters. It is interesting to explore how the various simulated models fare in comparison to the observations. Fig. A1 shows results of all models discussed in this paper compared with observed data from BSNIP. It seems that all models, even the most basic synthetic models described in §4.3, reproduce the observed relations between feature parameters quite well.

APPENDIX B: HEAD-ON COLLISION MODEL EXAMPLE SPECTRA

Head-on collision model spectra are compared to observed spectra. Two models were selected for each Branch type, and an SNID-assisted (Blondin & Tonry 2007) manual search was conducted for observed spectra with similar 6100Å and 5750Å features. The model spectra with the closest matching observed spectra are shown in Fig. B1. The location of each pair on the Branch plot is shown in Fig. B2.

APPENDIX C: SYNTHETIC MODELS WITH VARYING SI DENSITY PROFILE

Fig. 7 shows plots resulting from synthetic exponentially declining models with total density: $\rho(v) = \rho_0 e^{-v/v_0}$ up to a maximal velocity v_{\max} (see §4.3). Here we show results for synthetic models in which the total density profile remains constant (with $v_0 = 2,500$ km/s and $v_{\max} = 30,000$ km/s), while only the Si density profile is varied (either exponentially, varying v_0 or with a cutoff, varying v_{\max}). As can be seen in Fig. C1, the results are qualitatively very similar to Fig. 7.

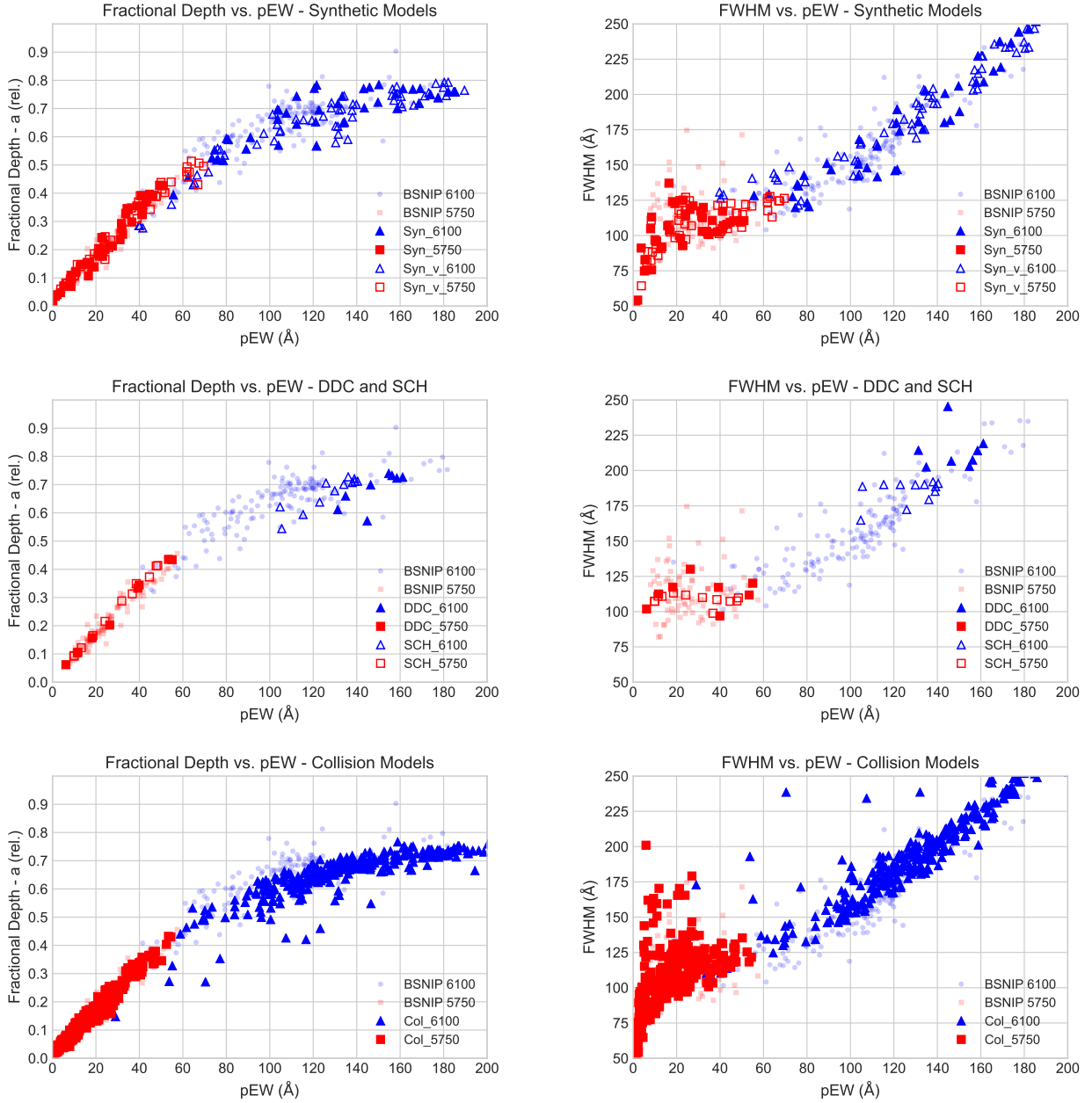


Figure A1. Relations between feature parameters in measured BSNIP data compared with simulated models. **Left:** Fractional depth vs. pEW for 6100Å and 5750Å features (blue and red dots). **Right:** Same for FWHM vs. pEW. See also §3.

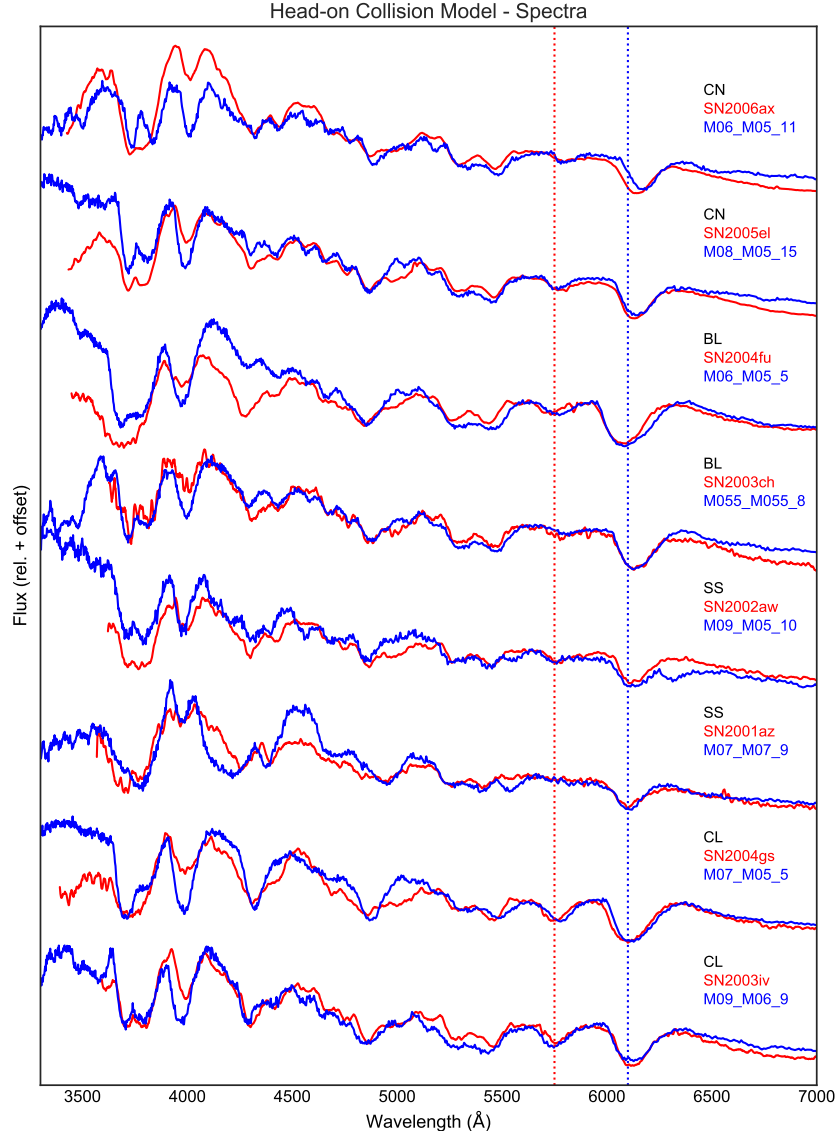


Figure B1. Example spectra from TARDIS simulations of head-on collision models are shown in blue. Two examples are given for each Branch type. Similar observed spectra are shown in red for comparison. The flux is scaled to match in the 6000Å region. Observed spectra were retrieved from the WISeREP repository (Yaron & Gal-Yam 2012).

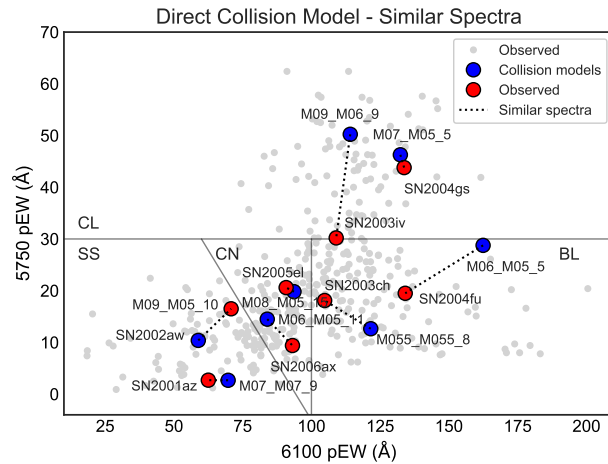


Figure B2. Branch plot showing the example head-on collision models and their corresponding similar observed events shown in Fig. B1.

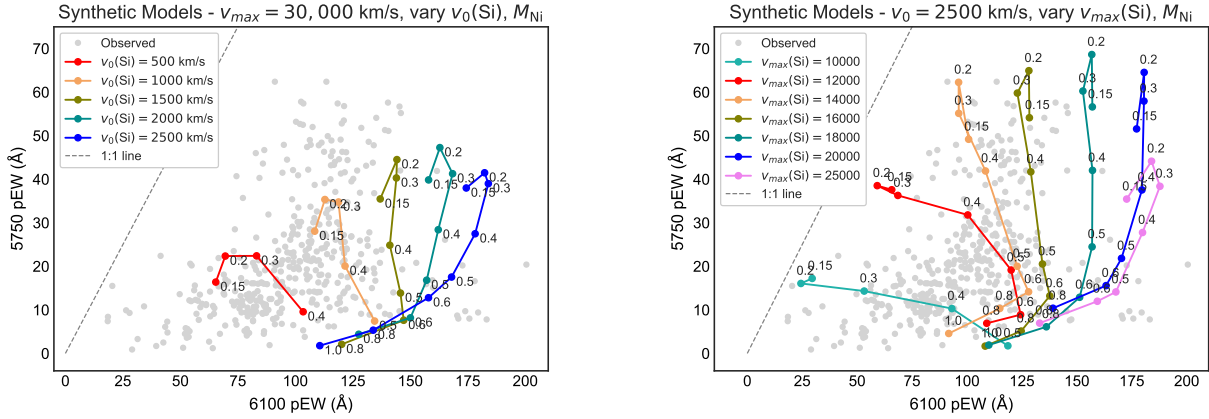


Figure C1. Simulated synthetic models with exponential density profiles of the form $\rho(v) = \rho_0 e^{-v/v_0}$, $\rho = 10^{-13}$ g cm $^{-3}$ at $V_{\text{ph}} = 9,000$ km/s at 18 days, overlaid on observed CfA, CSP and BSNIP data. In all models the total density profile remains constant (with $v_0 = 2,500$ km/s and $v_{\max} = 30,000$ km/s) and only the Si density profile is varied. Models with null or merging features have been omitted. $M(^{56}\text{Ni})$ is stated next to each point in units of M_{\odot} . L is computed from $M(^{56}\text{Ni})$ using Arnett’s rule $L_{\max} = 2.0 \times 10^{43} \times [M(^{56}\text{Ni})/M_{\odot}]$ erg/s. **Left:** Each line represents a constant Si density e-folding velocity v_0 with varying luminosity. **Right:** Each line represents a constant maximum Si density velocity cutoff v_{\max} with varying luminosity.